Construction of localized wave functions for a disordered optical lattice and analysis of the resulting Hubbard model parameters

S. Q. Zhou and D. M. Ceperley*

Department of Physics, University of Illinois at Urbana-Champaign, Urbana, Illinois 61801, USA

(Received 31 July 2009; published 4 January 2010)

We propose a method to construct localized single-particle wave functions using imaginary time projection and thereby determine lattice Hamiltonian parameters. We apply the method to a specific disordered potential generated by an optical lattice experiment and calculate for each instance of disorder the equivalent lattice model parameters. The probability distributions of the Hubbard parameters are then determined. Tests of localization and energy convergence are examined.

DOI: 10.1103/PhysRevA.81.013402 PACS number(s): 37.10.Jk, 71.15.−m, 71.23.An, 72.80.Ng

I. INTRODUCTION

Understanding the properties of disordered materials has a fundamental significance in condensed matter physics. Various kinds of disorder exist in real materials, but their disorder is difficult to characterize and control experimentally. Recently developed optical lattice techniques [1] have enabled the construction of a nearly perfectly controlled disordered potential and the measurement of properties of strongly correlated atoms in that potential provides an opportunity to compare quantitatively experimental results with parameter-free theoretical calculations. Bosonic atoms are particularly interesting because then Monte Carlo simulation is efficient.

In this article, we consider the problem of mapping a disordered single-body potential to a lattice model. By removing the high-energy states associated with the continuum, the Monte Carlo simulation becomes more efficient. Particularly, efficient algorithms have been developed [2,3] for lattice models. Consider the continuum Hamiltonian of N atoms with mass m moving in the external potential $U(\mathbf{r})$ and interacting with the pairwise potential energy $V(\mathbf{r}_\alpha - \mathbf{r}_\beta)$:

$$\hat{\mathcal{H}}_N = \sum_{\alpha=1}^{N}\left[\frac{\mathbf{p}_\alpha^2}{2m} + U(\mathbf{r}_\alpha)\right] + \sum_{\alpha<\beta} V(\mathbf{r}_\alpha - \mathbf{r}_\beta), \qquad (1)$$

where indices α and β label the atoms. On the other hand, the quantum mechanics of particles moving in a lattice is conveniently described in a basis of localized wave functions, such as the Wannier functions associated with a periodic potential. Using these localized functions, we can define an effective lattice Hubbard Hamiltonian. Written in second quantized notation it has the form

$$\hat{h} = -\sum_{\langle ij\rangle} t_{ij} a_i^\dagger a_j + \sum_i \epsilon_i n_i + \frac{1}{2}\sum_i u_i n_i(n_i - 1) - \sum_{\{ij\}} \tilde{t}_{ij} a_i^\dagger a_j + \frac{1}{2}\sum_{\langle ij\rangle} \tilde{u}_{ij} n_i n_j + \cdots, \qquad (2)$$

where i labels the single-particle states (lattice sites), $\langle ij\rangle$ denotes a nearest neighbor pair and $\{ij\}$ a next-nearest neighbor pair, t_{ij} and $\tilde{t}_{ij}$ are hopping coefficients, ϵ_i is the on-site energy, u_i is the on-site interaction, and $\tilde{u}_{ij}$ is the nearest-neighbor off-site interaction. (Terms such as next-nearest neighbor hopping and off-site interaction are often neglected.) Note that $\hat{\mathcal{H}}_N$ refers to the N-body Hamiltonian in continuous space and $\hat{h}$ to its equivalent on a lattice.

In a periodic potential, Wannier functions of a given band are related to the Bloch functions $\psi_{n\mathbf{k}}$ of the same band n by the unitary transformation

$$w_{ni}(\mathbf{r}) = w_n(\mathbf{r} - \mathbf{R}_i) = \frac{1}{\sqrt{N}}\sum_{\mathbf{k}} \psi_{n\mathbf{k}}(\mathbf{r}) e^{-i\mathbf{k}\cdot\mathbf{R}_i}. \qquad (3)$$

w_{ni} is localized around the lattice site $\mathbf{R}_i$ [4]. However, in the absence of periodicity, the concept of Wannier functions needs to be generalized. Two main types of generalizations exist in literature. The perturbative approach [5] assumes the existence of the band structure and thus is applicable to nearly periodic potentials. The variational approach [6–8] emphasizes the minimization of the spatial spread with respect to unitary transformations of a starting basis set, for example, the Wannier functions of a periodic potential.

In order to be useful, we would like the generalized Wannier functions to have the following properties. First, localization is required by the physical picture of particles hopping in the lattice. Second, a correct description of the low-energy density of states is necessary to capture the low-temperature physics. Third, for convenience, the orthogonality of the basis set is required to use commutation relations of creation and annihilation operators in the second quantized Hamiltonian. Finally, we would like the lattice Hamiltonian to be free of the sign problem so that quantum Monte Carlo calculations are efficient. This requires the off-diagonal elements to be nonpositive (i.e., $t_{ij} \geqslant 0$). Note that the original Hamiltonian $\hat{\mathcal{H}}_N$ has this property.

In Sec. II, we propose a method of constructing localized single-particle basis functions based on imaginary time evolution of localized basis functions: $w_i(0)$, where i labels the site.

$$|w_i(\tau)\rangle \equiv e^{-\tau\hat{\mathcal{H}}_1}|w_i(0)\rangle, \qquad (4)$$

where $\hat{\mathcal{H}}_1$ denotes the one-particle continuum Hamiltonian. This has the effect of suppressing the high-energy components but also spreading out the basis states. In Sec. III, results

*ceperley@illinois.edu

of the method are presented for the specific disorder probed experimentally.

II. METHOD

In constructing a lattice model, our goal is to coarse grain the description of the continuum system, so that instead of recording the precise position of an atom we only record which lattice site it occupies. We match up the lattice and the continuum models using the density matrix; we require that the low-temperature single-particle density matrix of the lattice model to be identical to that of the continuum system when one integrates over coordinate scales smaller than the lattice spacing. Use of the density matrix is motivated by the fact that the linear response of a system to an external perturbation, either an external field or a particle insertion, or to a coupling to another subsystem is determined by its one-body density matrix [9,10]. If we match the density matrices, the lattice system is guaranteed to have not only the same density distribution $n(\mathbf{r})$ and hopping properties, such as diffusion, but also the same response to external perturbations as the continuum system.

The unnormalized single-particle density matrix in the continuum system is defined by

$$\rho(\mathbf{r},\mathbf{r}';\tau)=\langle\mathbf{r}|e^{-\tau\hat{\mathcal{H}}_1}|\mathbf{r}'\rangle. \tag{5}$$

Let $w_i(\mathbf{r};0)$ be a localized basis which assigns atoms to lattice sites, for example, $w_i(\mathbf{r};0)=$ constant if $|\mathbf{r}-\mathbf{R}_i|$ is minimized with respect to i, that is, in the i^{th} Wigner-Seitz cell. Then a course-grained density matrix is defined as

$$\begin{aligned}S_{ij}(\tau)&=\langle w_i(0)|e^{-\tau\hat{\mathcal{H}}_1}|w_j(0)\rangle\\&=\int d\mathbf{r}\,d\mathbf{r}'w_i^*(\mathbf{r};0)\rho(\mathbf{r},\mathbf{r}';\tau)w_j(\mathbf{r}';0).\end{aligned} \tag{6}$$

Note that if $w_i(\mathbf{r};0)$'s are chosen to be everywhere positive, all elements of the lattice density matrix S_{ij} are also positive and can be used directly in a lattice quantum Monte Carlo (QMC) calculation to define the probability of a path on the lattice. We now want to construct a single-particle Hamiltonian, which when solved gives $S_{ij}(\tau)$ for large τ, or in matrix notation to determine $\hat{h}$ such that

$$\hat{S}(\tau)=e^{-\tau\hat{h}}. \tag{7}$$

(Note that S is Hermitian and positive definite, so h exists uniquely.) Formally, the solution $\hat{h}=-\tau^{-1}\ln\hat{S}(\tau)$ may have some τ dependance and not necessarily have the other properties mentioned previously. Differentiating Eq. (7) with respect to τ and multiplying on the right and left by $\hat{S}^{-1/2}$, we find an expression for h in terms of S:

$$\hat{h}=-\hat{S}^{-\frac{1}{2}}\frac{d\hat{S}}{d\tau}\hat{S}^{-\frac{1}{2}}-\int_0^\tau e^{(\frac{\tau}{2}-\lambda)\hat{h}}\left(\frac{d\hat{h}}{d\tau}\right)e^{(\lambda-\frac{\tau}{2})\hat{h}}d\lambda. \tag{8}$$

If we assume that h becomes τ independent as $\tau\to\infty$, we can neglect the second term on the right-hand side and find

$$\hat{h}=-\hat{S}^{-\frac{1}{2}}\frac{d\hat{S}}{d\tau}\hat{S}^{-\frac{1}{2}}. \tag{9}$$

Consider the eigenfunction expansion of the continuum density matrix:

$$\rho(\mathbf{r},\mathbf{r}';\tau)=\sum_\alpha\phi_\alpha^*(\mathbf{r})\phi_\alpha(\mathbf{r}')e^{-\tau E_\alpha}, \tag{10}$$

where E_α and ϕ_α are the one-particle eigenvalues and eigenfunctions of the continuum Hamiltonian. For a sufficiently large τ, and for a system with a gap, only states below the gap will survive. If there are N such states, it is clear that we will capture the density of states with exactly N basis functions w_i. Now let us define the orthogonalized basis by splitting up the density operator

$$\exp(-\tau\hat{\mathcal{H}}_1)=\exp\left(-\frac{1}{2}\tau\hat{\mathcal{H}}_1\right)\exp\left(-\frac{1}{2}\tau\hat{\mathcal{H}}_1\right) \tag{11}$$

and having it act partially to the left and the right in Eq. (6). Combining Eq. (6) and Eq. (9), we obtain an expression for the model Hamiltonian:

$$\begin{aligned}h_{ij}&=\sum_{kl}S_{ik}^{-\frac{1}{2}}(\tau)\langle w_k(\tau/2)|\hat{\mathcal{H}}_1|w_l(\tau/2)\rangle S_{lj}^{-\frac{1}{2}}(\tau)\\&=\langle\tilde{w}_i(\tau/2)|\hat{\mathcal{H}}_1|\tilde{w}_j(\tau/2)\rangle,\end{aligned} \tag{12}$$

where $w_i(\tau)=e^{-\tau\hat{\mathcal{H}}_1}w_i(0)$ are the nonorthonormalized basis functions at time τ and $\tilde{w}(\tau/2)=\hat{S}^{-1/2}(\tau)w(\tau/2)$ are the orthonormalized basis functions because

$$S_{ij}(\tau)=\langle w_i(\tau/2)|w_j(\tau/2)\rangle \tag{13}$$

is the overlap matrix. This is known as *Löwdin orthogonalization* [11].[1]

The imaginary time evolution is equivalent to a diffusion process with sinks or sources determined by the potential $U(\mathbf{r})$. Without a potential present, an initially localized distribution will spread out as $\sqrt{\tau}$ as a function of imaginary time. When the wave packet (or basis function) $|w_i(\tau)\rangle\equiv e^{-\tau\hat{\mathcal{H}}_1}|w_i(0)\rangle$ encounters the regions of high potential energy separating the lattice sites, its diffusion will stop, until it tunnels through to the next site. If the assumption of temperature independence,

$$\lim_{\tau\to\infty}\left(\frac{d\hat{h}}{d\tau}\right)=0, \tag{14}$$

is correct, according to Eq. (12) the orthogonalized basis $\hat{S}^{-1/2}(2\tau)|w_i(\tau)\rangle$ converges at large τ. Instead of taking the logarithm of the reduced density matrix Eq. (7), we choose to construct the lattice Hamiltonian from Eq. (9) for two reasons. First, numerical tests show that Eq. (9) converges faster than $-\frac{1}{\tau}\ln\hat{S}$ as τ increases. Second, the explicit construction of basis functions enables us to calculate the interaction terms in the second quantized many-body Hamiltonian. Finally, use of Eq. (9) instead of Eq. (7) gives energy levels which lie above their counterparts in the continuum system.

The choice of the initial basis functions $w_i(\mathbf{r};0)$ is to some extent arbitrary, as long as they are non-negative and localized. It is reasonable to suppose that there should be one basis function for each lattice site, at least for weak disorder. In this

[1]This is mathematically equivalent to the procedure for periodic potentials introduced by Wannier [4].

work, where the disordered potential is an order of magnitude smaller than the lattice potential, we chose to set $w_i(\mathbf{r};0) = \sigma^{-\frac{3}{2}}$ inside a cube of side σ centered on $\mathbf{R}_i$.

When the disordered potential becomes as strong as the lattice potential, the original lattice bands can strongly overlap, and this simple choice may be inadequate. Multiband effects would necessitate the inclusion of more than one basis function for each lattice site. Also one might want to use the freedom to choose the locations of the basis functions, by concentrating more basis functions in regions of low potential energy. We do not explore these issues further in this article because the disorder we consider is weak.

A. Algorithm for imaginary time projection and orthogonalization

To apply the imaginary time evolution to the construction of localized wave functions and thereby to extract microscopic parameters of the corresponding lattice model, we start with N initial trial wave functions, each of which is well localized in one lattice cell. Each wave function is *independently* evolved over a sufficiently long imaginary time. The set of N wave functions are then transformed into an orthonormal basis.

To perform the imaginary time evolution, consider the Trotter formula [12]

$$e^{-\beta\hat{\mathcal{H}}_1} = \lim_{n\to\infty}\left(e^{-\frac{\beta}{n}\hat{T}}e^{-\frac{\beta}{n}\hat{U}}\right)^n. \tag{15}$$

In a coordinate representation, a single step of imaginary time τ can be written as

$$\begin{aligned} w(\mathbf{r},t+\tau) &= \int d^3\mathbf{r}'\langle\mathbf{r}|e^{-\tau\hat{\mathcal{H}}_1}|\mathbf{r}'\rangle w(\mathbf{r}',t) \\ &= \left(\frac{m}{2\pi\hbar\tau}\right)^{3/2}\int d^3\mathbf{r}' e^{-\frac{m}{2\hbar\tau}(\mathbf{r}'-\mathbf{r})^2}e^{-\frac{\tau U(\mathbf{r}')}{\hbar}}w(\mathbf{r}',t). \end{aligned} \tag{16}$$

This integral is a convolution and can be efficiently evaluated by fast Fourier transform (FFT)

$$w(\mathbf{r},t+\tau) = T_{\mathrm{FF}}\left[e^{-\frac{\tau\hbar\mathbf{k}^2}{2m}}f_{\mathbf{k}}\right], \tag{17}$$

where $f_{\mathbf{k}}$ is defined as an inverse-Fourier transform

$$f_{\mathbf{k}} = {T_{\mathrm{FF}}}^{-1}\left[e^{-\frac{\tau U(\mathbf{r})}{\hbar}}w(\mathbf{r},t)\right]. \tag{18}$$

where T_{FF} denotes fast Fourier transform. We can also take advantage of the localization of $w(\mathbf{r})$: it is vanishingly small away from its initial site, so that we only store its values in a cube enclosing the region in which the wave function is nonzero. When doing the second FFT, Eq. (17), we add a buffer layer outside the cube with thickness chosen so that the localization region of the evolved function over one imaginary time step does not exceed the cube in which FFT is performed; the thickness is proportional to $\sqrt{\tau/m}$. We periodically examine the evolved basis set to determine if the cube can be made smaller. A common normalization factor is required for all basis functions occasionally to avoid numerical overflow or underflow.

Equation (9) demands orthogonalization of the basis set. Löwdin orthogonalization preserves, as much as possible, the localization and symmetry of the original nonorthogonal basis states. In terms of the overlap matrix, we construct a set of orthogonalized states:

$$|\tilde{w}_i\rangle = \sum_j (S^{-1/2})_{ij}|w_j\rangle. \tag{19}$$

No other set of orthonormal states generated from the space spanned by the original nonorthogonal set of states resembles the original set more closely, in the least-squares sense, than does the Löwdin set [13]. Explicitly, Löwdin orthogonalization minimizes the expression

$$\phi(\hat{T}) \equiv \sum_{i=1}^{N}\|\hat{T}w_i - w_i\|^2 \tag{20}$$

over all linear transformations $\hat{T}$ which transform the original nonorthonormal set of states $|w_i\rangle$ into an orthonormal set of states $|\tilde{w}_i\rangle$:

$$\langle\tilde{w}_i,\tilde{w}_j\rangle \equiv \langle\hat{T}w_i,\hat{T}w_j\rangle = \delta_{ij}. \tag{21}$$

For efficiency, this procedure can be done in an iterative fashion. Because the original nonorthogonal set of wave functions are localized, the overlap matrix S_{mn} has the form of the identity matrix plus a small off-diagonal part,

$$S_{ij} = \delta_{ij} + A_{ij}, \tag{22}$$

where the diagonal elements of A are zero and the off-diagonal elements $|A_{ij}| \ll 1$. This enables us to perform Löwdin orthogonalization iteratively by repeated application of the approximate inverse square root of the overlap matrix

$$(\hat{S}^{-1/2})_{ij} \approx \delta_{ij} - \tfrac{1}{2}A_{ij} \tag{23}$$

to the nonorthogonal basis set by updating the overlap matrix at each step [14]. Hence the basis set is iterated as

$$\tilde{w} \leftarrow \left(\mathbf{1} - \tfrac{1}{2}\hat{A}\right)\tilde{w} \tag{24}$$

until convergence is reached, $|\hat{A}| \sim 0$. The convergence of the overlap matrix to identity matrix is geometric.

The iterative scheme is efficient for large systems because the basis sets are sparse. The computation time of this algorithm is linear in the number of lattice sites, that is, the complexity is proportional to

$$(\#\text{ of steps})\, Mn\ln n, \tag{25}$$

where M is the number of lattice sites and n is the number of mesh points for each basis function.

B. Hubbard parameters

Once the orthogonalized basis set has been constructed, the effective lattice Hamiltonian is obtained. For convenience we drop the τ dependance. According to Eq. (12), the single-particle Hubbard parameters are calculated as the on-site energies,

$$\epsilon_i = \int \tilde{w}_i^*(\mathbf{r})\hat{\mathcal{H}}_1\tilde{w}_i(\mathbf{r})d^3\mathbf{r}, \tag{26}$$

and the hopping coefficients,

$$t_{ij} = -\int \tilde{w}_i^*(\mathbf{r})\hat{\mathcal{H}}_1\tilde{w}_j(\mathbf{r})d^3\mathbf{r}. \tag{27}$$

The interaction term is computed from first-order perturbation theory in V. In the case of a contact interaction with the scattering length a_s we find for u:

$$u_i = \frac{4\pi a_s \hbar^2}{m} \int |\tilde{w}_i(\mathbf{r})|^4 d^3\mathbf{r} \tag{28}$$

and the off-site interaction

$$\tilde{u}_{ij} = \frac{4\pi a_s \hbar^2}{m} \int |\tilde{w}_i(\mathbf{r})|^2 |\tilde{w}_j(\mathbf{r})|^2 d^3\mathbf{r}. \tag{29}$$

C. Measures of localization and energy

Several quantities can be used to characterize the localization and accuracy of the basis set. The spatial spread $\Omega_w \equiv \langle r^2 \rangle_w - \langle \mathbf{r} \rangle_w^2$ quantifies the localization of a wave function.

The off-site integral $\tilde{u}_{ij}$ measures the spatial overlap between a pair of basis states. If it is small relative to t_{ij} and the Hubbard U, the approximation of keeping only the on-site interaction in the lattice model is appropriate. Its rms value over all nearest-neighbor pairs measures the whole basis set.

The convergence rate of the $N \times N$ matrix of the single-particle lattice Hamiltonian is measured by the time derivatives of its N eigenvalues' $E^{(i)}_{\text{lattice}}$'s,

$$\Gamma = \frac{1}{N} \sum_i \left| \frac{d}{d\tau} E^{(i)}_{\text{lattice}} \right|. \tag{30}$$

To determine the accuracy of the basis set we compare $E^{(i)}_{\text{lattice}}$'s with the lowest N eigenvalues $E^{(i)}_{\text{exact}}$ of the original continuum Hamiltonian $\hat{\mathcal{H}}_1$ estimated from

$$E^{(i)}_{\text{exact}} = E^{(i)}_{\text{lattice}}(\tau \to \infty). \tag{31}$$

The *worst case error* is defined as

$$e_{\text{lattice}} \equiv \max_i \left| E^{(i)}_{\text{lattice}} - E^{(i)}_{\text{exact}} \right|. \tag{32}$$

We did the same estimate for the lattice Hamiltonian that has only nearest-neighbor hopping terms.

III. RESULTS FOR A DISORDERED LATTICE

We now test the numerical method on a disordered lattice potential created in the White *et al.* experiment [1], ^{87}Rb atoms are trapped in a background cubic lattice potential created by lasers with wave vector $k = \frac{\pi}{a}$. First we discuss the model without the disorder. The periodic background potential is

$$U_L(\mathbf{r}) = -S_L \sum_{i=1}^{3} \cos\left(\frac{2\pi \mathbf{n}_i \cdot \mathbf{r}}{a} \right), \tag{33}$$

where $\mathbf{n}_i$ are three mutually orthogonal unit vectors. In the following we express all energies in terms of the recoil energy $E_R = \frac{\hbar^2 k^2}{2m} = \frac{\hbar^2 \pi^2}{2ma^2}$ and all lengths in terms of the lattice spacing $a = 406$ nm. In these units the single-particle Hamiltonian is

$$\mathcal{H}_1 = -\frac{\nabla^2}{\pi^2} + \frac{U(\mathbf{r})}{E_R}, \tag{34}$$

where $U(\mathbf{r}) = U_L(\mathbf{r})$ in the absence of disorder. The problem of a single particle moving in this potential can be solved analytically [15]. We compared the imaginary time projected states with the results from exact diagonalization using the same spatial grid of 8^3 mesh points per lattice cell. We find perfect agreement in the limit of zero time step.

We constructed a disordered potential to match the experiment [1] as closely as possible. A disordered speckle field $U_D(\mathbf{r})$ is produced by a laser beam with phases randomized by a diffuser and has the form

$$U_D(\mathbf{r}) \propto SD \times \left| T_{\text{FF}} \left[\Theta\left(d^2 - q_x^2 - q_y^2\right) \times \exp\left\{ -\frac{q_x^2 + q_y^2}{w^2} + i\gamma z \left(q_x^2 + q_y^2\right) + i\phi\left(q_x, q_y\right) \right\} \right] \right|^2, \tag{35}$$

where Θ is an aperture disc with radius $d = 0.66k$ and $w = 2.16k$ is the waist of the Gaussian beam, $\gamma = 0.1a$ characterizes its radius of curvature, $\phi(q_x, q_y)$ is an uncorrelated random phase uniformly distributed in $[0, 2\pi)$ and the Fourier transform (FT) is performed in the two-dimensional (q_x, q_y) space. We normalize the field so that $\langle U_D(\mathbf{r}) \rangle = S_D$. Detailed derivations can be found in Goodman [16]. The spatial autocorrelation $\langle U_D(\mathbf{r}) U_D(\mathbf{r}') \rangle$ has a correlation length $\sim 1.29a$, that is, slightly larger than the lattice spacing. In addition, the orientation of laser speckles in White *et al.* [1] does not coincide with the lattice axes; the z axis in Eq. (35) points along $\frac{1}{2}\mathbf{n_1} + \frac{1}{2}\mathbf{n_2} + \frac{1}{\sqrt{2}}\mathbf{n_3}$ of the optical lattice. The total external potential is a superposition of the periodic lattice potential and the speckle potential $U(\mathbf{r}) = U_L(\mathbf{r}) + U_D(\mathbf{r})$. In the following, S_L and S_D are given in units of E_R.

The ^{87}Rb scattering length is chosen to be $a_s = 100a_0 = 5.29$ nm, where $a_0 = 0.0529$ nm is the Bohr radius. In units of the lattice spacing, $a_s = 0.013a$.

To investigate the evolution of lattice Hamiltonian Eq. (9), at every step of the imaginary time, the basis set is orthonormalized before constructing the Hamiltonian matrix and calculating the energies $E^{(i)}_{\text{lattice}}$. Then the basis set is evolved using the previous basis set before orthonormalization; each basis function is evolved independently.

To illustrate the convergence of the matrix elements of the lattice Hamiltonian, the evolution diagram of an on-site energy on one particular site and a nearest-neighbor hopping coefficient on one particular bond for $S_L = 14$ and $S_D = 1$ are shown in Fig. 1. We characterize the localization of the basis functions by the average nearest-neighbor off-site integral $\tilde{u}_{ij}$, which measures the spatial overlap between a pair of nearest-neighbor basis functions. Figure 2 shows the evolution diagrams of the average on-site interaction u_i and the average off-site interaction $\tilde{u}_{ij}$, which are also converging at large imaginary time. The limiting value of the off-site interaction is $4 \sim 5$ orders of magnitude smaller than that of the on-site interaction, which means that the basis functions are still localized at large imaginary time. Note that although the imaginary time projection operator $e^{-\tau \hat{\mathcal{H}}_1}$ spreads out the basis states, Löwdin orthogonalization operator $\hat{S}^{-1/2}$ restores their localization.

To illustrate the effect of Löwdin orthogonalization on localization, the evolution diagram for $S_L = 14$ and $S_D = 1$ is shown in Fig. 3 by including the off-site integral of the set

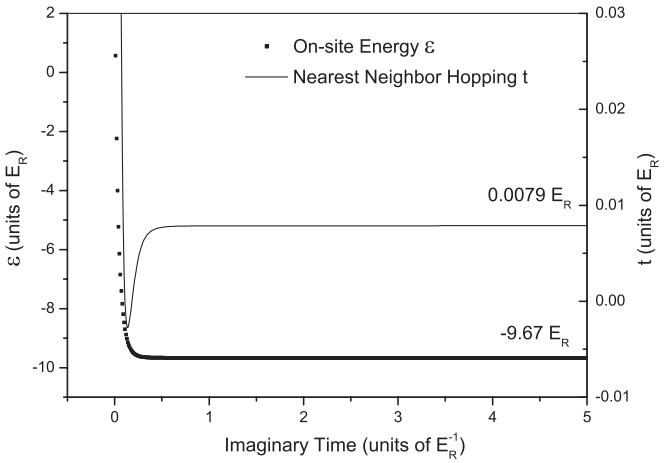

FIG. 1. Evolution diagram of an on-site energy (left scale) and a nearest-neighbor hopping coefficient (right scale) in a lattice for $S_L = 14$ and $S_D = 1$. At large imaginary time τ, these two matrix elements approach constant values.

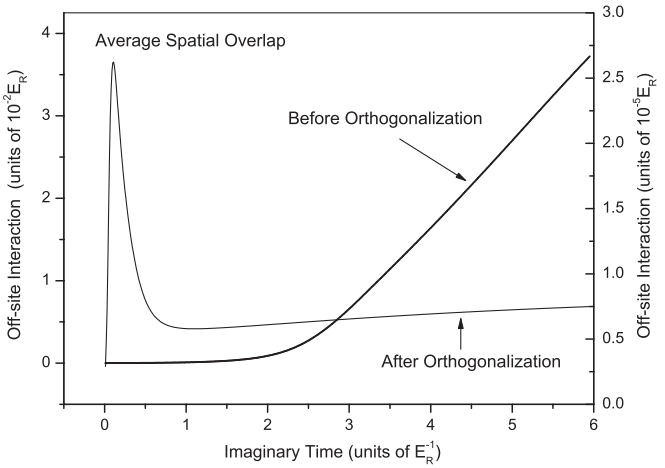

FIG. 3. Evolution diagram of the average nearest-neighbor off-site interaction $\tilde{u}$ before orthogonalization (left scale) and after orthogonalization (right scale) for $S_L = 14$ and $S_D = 1$.

before orthogonalization. It can be seen from the graph that the Löwdin procedure helps to localize the basis functions $w(\tau)$.

The localization characterized by the spatial spread Ω_w and drift D_w is shown in Fig. 4. The maximum value among all basis functions is chosen to measure the whole basis set. As shown in the graph, the values that these two quantities asymptote to at large time are small compared to the lattice constant, which signifies that the basis functions are localized. This result indicates that for weak disorder, the basis set of wave functions produced by imaginary time evolution which span the lowest-energy manifold is indeed sufficiently localized around the original lattice sites of the simple cubic lattice.

The convergence rate Γ of eigen-energies of the lattice Hamiltonian is shown in Fig. 5. It can be seen from the graph that the effective lattice Hamiltonian becomes temperature independent at low temperatures. It is also illuminating to look at the evolution diagram of the worst-case error, Eq. (32), as shown in Fig. 6 where the exact eigen-energies are estimated by

$$E^{(i)}_{\text{exact}} = E^{(i)}_{\text{lattice}}\left(\tau = 8E_R^{-1}\right). \tag{36}$$

We compared the worst-case error in energy for the nearest-neighbor model ($\tilde{t} = 0$) versus the full lattice model. The spatial overlap between basis functions remains negligible at the early stage so that the nearest-neighbor model has almost the same spectrum as the full lattice model; the error in energy is reduced as imaginary time evolves. The error in the eigen-energy of the full lattice model decreases as the time step goes to zero, whereas a finite error persists in the nearest-neighbor model because the next-nearest-neighbor

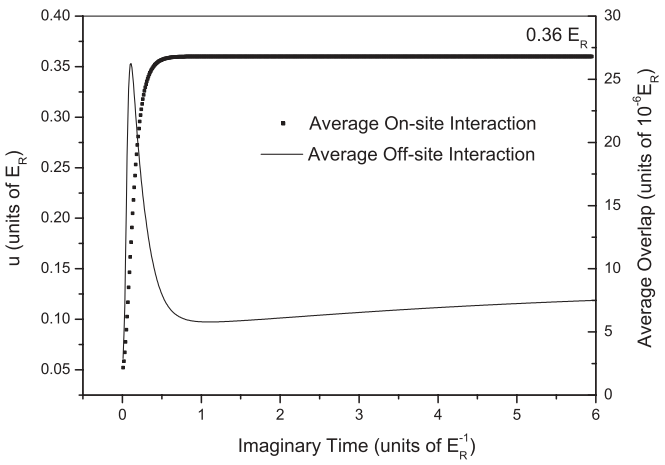

FIG. 2. Evolution diagram of the average on-site interaction u (left scale) and the average nearest-neighbor off-site interaction $\tilde{u}$ (right scale) for $S_L = 14$ and $S_D = 1$. Note that $\tilde{u}$ measures the localization of a pair of basis functions. The diagram shows that the limiting value of $\tilde{u}$ is $4 \sim 5$ orders of magnitude smaller than that of u, which indicates that the basis functions at large imaginary time are still localized.

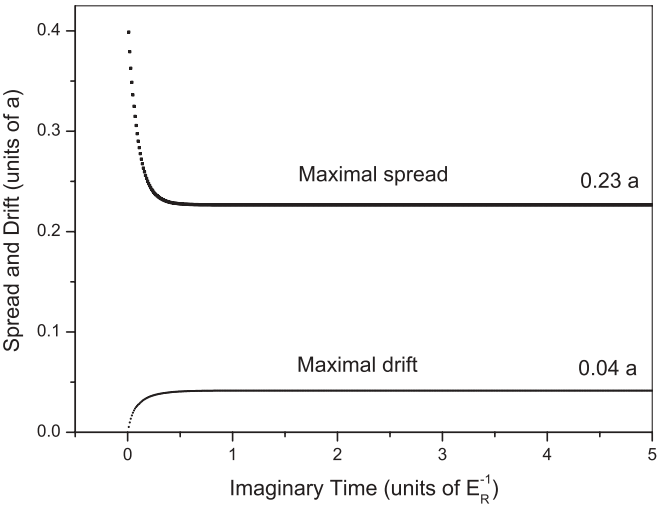

FIG. 4. Evolution diagram of the maximum spatial spread and drift (average deviation from the initial position) in units of the lattice constant for $S_L = 14$ and $S_D = 1$. The values that these two quantities approach at large imaginary time are small compared to the lattice constant a, which means that the localization of the basis functions is preserved.

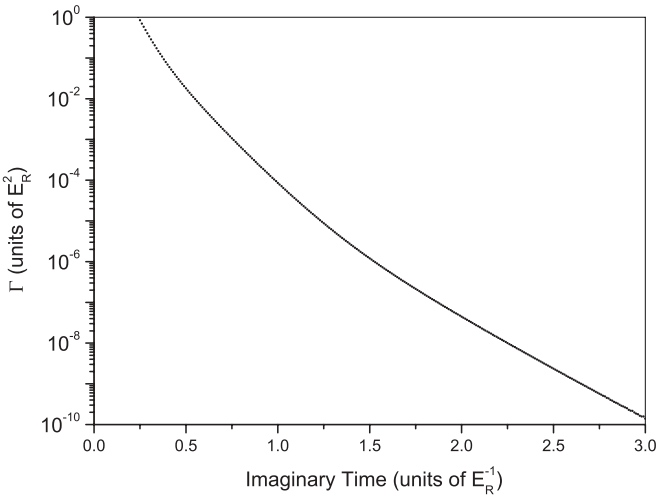

FIG. 5. Convergence rate Γ of eigen-energies for $S_L = 14$ and $S_D = 1$ shown in log-scale.

hopping terms are neglected. Note that this error is less than $10^{-4}E_R$, which is the same order of magnitude of the next-nearest-neighbor hopping coefficients.

To explain how it is possible to suppress the energy of the original localized basis set before causing significant delocalization, it is useful to look at the single-particle density of states (DOS). In particular, we are interested in whether the gap between bands persists in the presence of disorder. Figure 7 shows the DOS in the disordered lattice. Fifteen samples, each from a 5^3 lattice for each disorder strength, were used to determine the DOS. It can be seen from the plot that the lowest band is broadened and skewed by the disorder; there remains a minimum in the density of states between the first band and the second band (pseudo-gap). It is the existence of such a gap that enables us to project out the high-energy

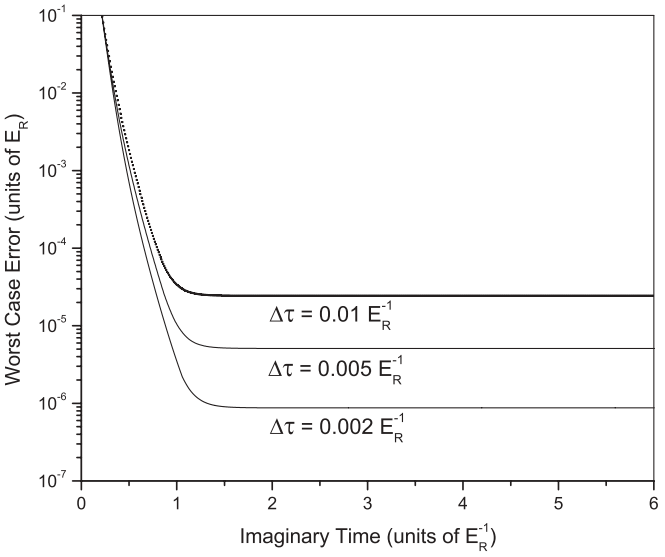

FIG. 6. Imaginary time evolution of the worst-case error in energy for $S_L = 14$ and $S_D = 1$, shown in log-scale. Three different imaginary time steps, $\Delta\tau = 0.01E_R^{-1}, 0.005E_R^{-1}$, and $0.002E_R^{-1}$, were chosen to demonstrate the finite time step error.

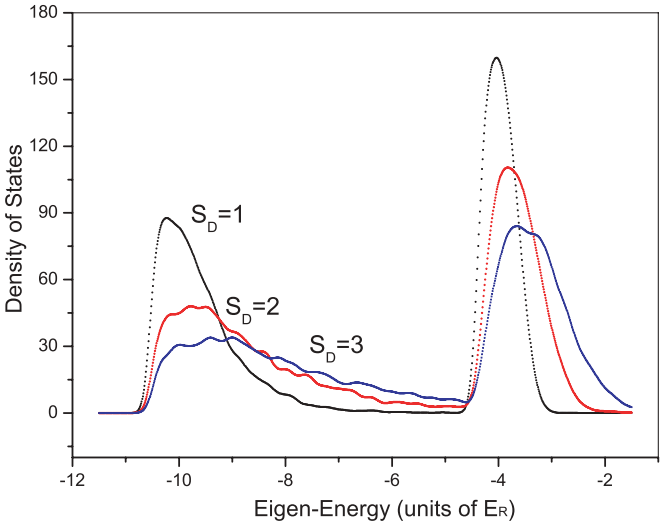

FIG. 7. (Color online) Density of states for a single particle in a disordered lattice with $S_L = 14$ and varying amounts of disorder: $S_D = 1, 2, 3$.

components in the initial set of trial states before delocalization sets in.

For values of $S_D \geqslant 2$ ($S_L = 14$), we found rare cases where the highest eigen-energy does not converge to the lowest possible exact solution. Because each wave function is evolved independently before the orthogonalization is performed, the basis set becomes numerically singular at large imaginary time. This problem is more severe for strongly disordered potentials where the highest several lattice eigen-states may fail to converge into the lowest energy manifold before the instability sets in.

IV. STATISTICS OF HUBBARD PARAMETERS

We now discuss the statistical properties of the calculated Hubbard parameters. These are shown in Figs. 8–12 for $S_L = 14$ and $S_D = 1$. About 1000 samples of 6^3 sites are used to construct the probability distributions of Hubbard parameters.

Figure 8 shows the probability distribution of the on-site energy ϵ_i for $S_D = 1$ and $S_L = 14$. The distribution is skewed with a steep onset at low energy and a tail at high energy. We fit the distribution to an exponential decay function,

$$P(\varepsilon) \sim \exp(-\varepsilon/\Gamma), \tag{37}$$

for $\varepsilon > -10.5\ E_R$, finding $\Gamma \approx 0.97\ E_R$ for $S_D = 1$ and $S_L = 14$. Note that the disorder potential is always positive, so that the on-site energy is greater than its value for the periodic lattice which is $-10.58\ E_R$ for this value of S_L.

Hopping coefficients t_{ij} characterize the mobility of the atoms. Recall that negative values of t will cause difficulty in QMC calculations. Figure 9 shows the probability distribution of nearest-neighbor hopping coefficients. This distribution is asymmetrically centered around its value $8 \times 10^{-3}\ E_R$ for the periodic potential with a width

$$\frac{\delta t}{\langle t \rangle} = 0.15. \tag{38}$$

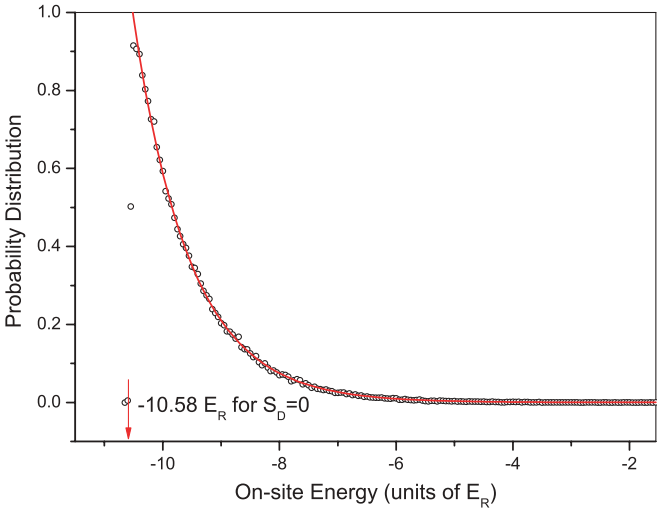

FIG. 8. (Color online) Probability distribution of the on-site energy for $S_L = 14$ and $S_D = 1$. The line is a fit to an exponential function.

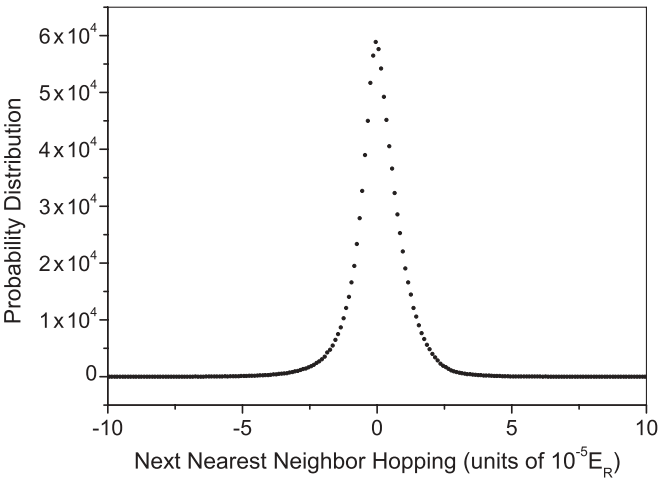

FIG. 10. Probability distribution of the next-nearest-neighbor hopping for $S_L = 14$ and $S_D = 1$. This distribution is symmetrically centered around zero.

In 10^6 sampled bonds, only positive $t_{\langle ij\rangle}$ were found. For $S_L = 14$ and for $0.05 \leqslant S_D \leqslant 1$, $\delta t/\langle t\rangle$ ranges from 10^{-2} to 10^{-1}.

Figure 10 shows the probability distribution of next-nearest neighbor hopping coefficients. This distribution is symmetrically centered around zero with a width $w = 1.25 \times 10^{-5}\ E_R$ and about 2 orders of magnitude smaller than nearest-neighbor hopping. Note that in the clean limit, the next-nearest-neighbor hopping coefficient is exactly zero for the simple cubic lattice by symmetry. Setting $\tilde{t} = 0$ changes the resulting single-particle energies by a maximum of $2 \times 10^{-5}\ E_R$.

Figure 11 shows the probability distribution of the Hubbard U, which is characterized by its narrow peak roughly centered around the value of u in the periodic limit ($0.36\ E_R$) with a 1% relative width. We fit this distribution to the Laplace function

$$P(u) = \frac{1}{2\Delta} \exp\left(-\frac{|u - u_0|}{\Delta}\right), \tag{39}$$

with $u_0 \approx 0.36\ E_R$ and $\Delta = 2 \times 10^{-3}\ E_R$. For $S_L = 14$ and for $10^{-2} \leqslant S_D \leqslant 1$, $\delta u/\langle u\rangle$ ranges from 10^{-4} to 10^{-2}. Hence one can assume that the on-site interaction is roughly constant even in the presence of disorder. Figure 12 shows the probability distribution of nearest-neighbor off-site interaction $\tilde{u}$. We observe that the magnitude of off-site interactions is almost 4 orders of magnitude smaller than the on-site interaction, evidently negligible in the many-body interacting Hamiltonian.

On-site energies are usually assumed to be almost uncorrelated between different sites. We calculated the nearest-neighbor covariance function. For $S_L = 14$ and $S_D = 1$, with

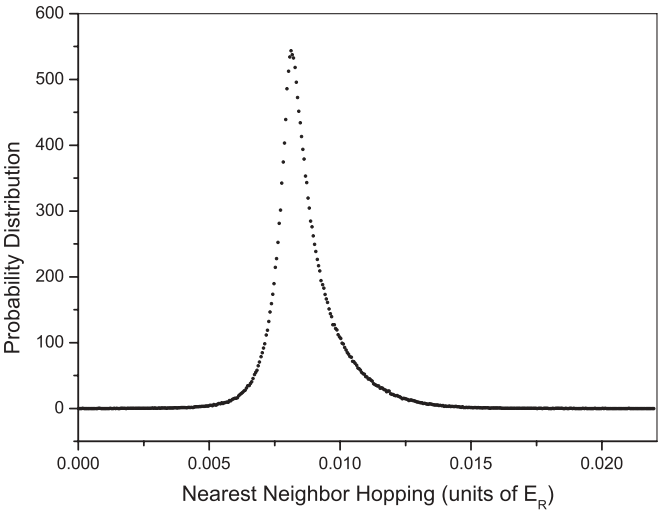

FIG. 9. Probability distribution of the nearest-neighbor hopping with $S_L = 14$ and $S_D = 1$. This is a predominantly positive asymmetric distribution.

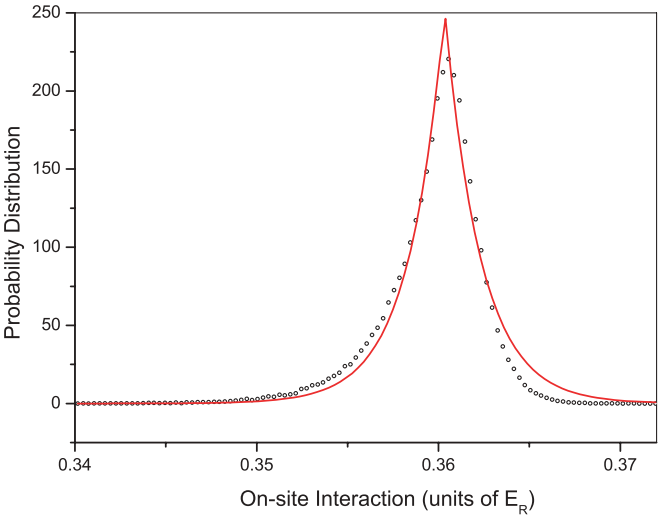

FIG. 11. (Color online) Probability distribution of the on-site interaction, that is, Hubbard U, for $S_L = 14$ and $S_D = 1$. The line is a fit to a Laplace function.

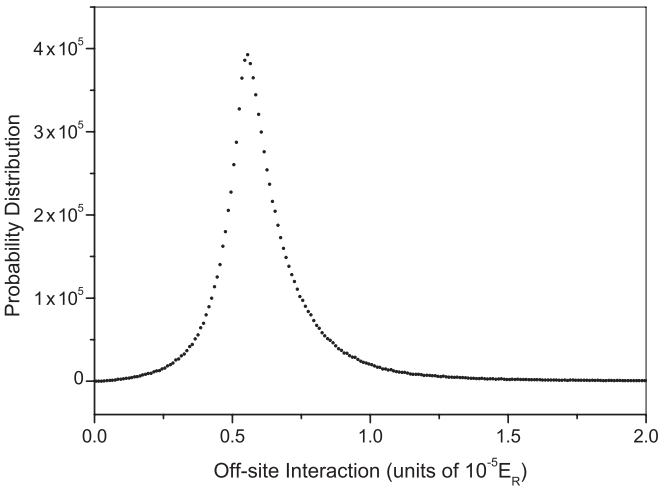

FIG. 12. Probability distribution of the nearest-neighbor off-site interaction for $S_L = 14$ and $S_D = 1$.

$\langle ij \rangle$ nearest-neighbor pairs,

$$\frac{\langle \varepsilon_i \varepsilon_j \rangle - \langle \varepsilon_i \rangle \langle \varepsilon_j \rangle}{\langle \varepsilon^2 \rangle - \langle \varepsilon \rangle^2} \approx 0.49. \tag{40}$$

The ε_i's are correlated between nearest-neighboring sites for this disordered potential.

Figure 13 shows the correlation pattern between the on-site energy difference of nearest-neighboring sites and the hopping coefficient. Fit to this joint distribution gives $\langle t_{\langle ij \rangle} \rangle - t_0 \sim \langle |\epsilon_i - \epsilon_j| \rangle^\delta$ with $\delta = 1.05$. Note that in White *et al.* [1], the orientation of laser speckles points along $\frac{1}{2}\mathbf{n_1} + \frac{1}{2}\mathbf{n_2} + \frac{1}{\sqrt{2}}\mathbf{n_3}$. The insert of Fig. 13 displays the correlation pattern for bonds in the $\mathbf{n_3}$ direction if the longitudinal direction of the speckles is aligned with the $\mathbf{n_3}$ axis of the lattice. This illustrates the anisotropy of laser speckles.

The characteristics of the speckle field is reflected in other aspects of the parameters. According to the orientation of laser

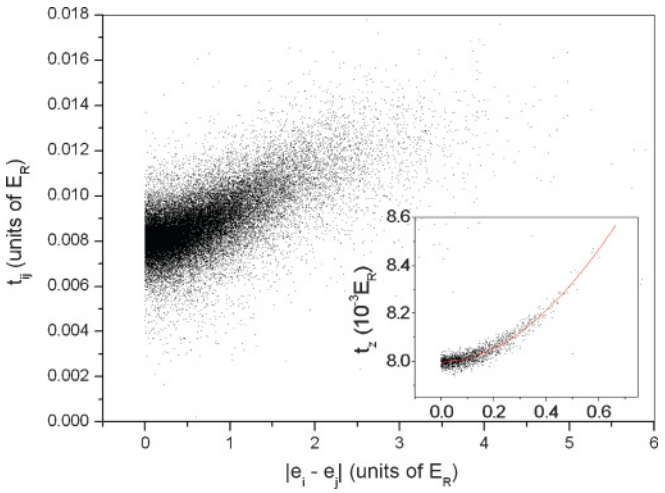

FIG. 13. (Color online) Correlation between the on-site energy difference and hopping coefficient between nearest-neighbor sites for $S_L = 14$ and $S_D = 1$. The insert displays the correlation pattern for bonds in the $\mathbf{n_3}$ direction if the longitudinal direction of the speckles is aligned with the $\mathbf{n_3}$ axis of the lattice. The line in the insert is a fit to a power function.

TABLE I. Anisotropy of speckles for $S_L = 14$. The speckle strength S_D is in units of E_R and the hopping coefficients are in units of 10^{-3} E_R. Statistical errors are smaller than the number of digits shown.

S_D	$\langle t_x \rangle$	$\langle t_y \rangle$	$\langle t_z \rangle$
0.050	8.00	8.00	8.00
0.100	8.02	8.02	8.01
0.250	8.10	8.10	8.07
0.375	8.20	8.20	8.16
0.500	8.32	8.33	8.26
0.750	8.59	8.60	8.48
1.000	8.72	8.73	8.57

speckles with respect to the lattice axes, we should expect that the average hopping coefficient along $\mathbf{n_1}$ and $\mathbf{n_2}$ to be equal and the hopping along $\mathbf{n_3}$ to be different. As shown in Table I, $\langle t_z \rangle$ differs from $\langle t_{x,y} \rangle$ because of the cylindrical symmetry of the speckle. However, the difference is small because the correlation length of the speckle is only slightly larger than the lattice spacing, such that the nearest-neighbor hopping is not sensitive to the anisotropy induced by the speckle.

In Fig. 14 the variation of the distribution widths of all four Hubbard parameters versus speckle intensity is shown for $S_L = 14$. Figure 14(a) shows the dependence of the width

$$\sigma_\epsilon = \langle \sqrt{(\epsilon_i - \langle \epsilon_i \rangle)^2} \rangle$$

for the on-site energy on the disorder strength S_D for $S_L = 14$. It can be seen from the graph that σ increases linearly with the disorder strength, approximately equal to the speckle potential shift. Hence, the width is an appropriate measure of the disorder strength. The linear fit of this functional dependence gives $\sigma_\epsilon = 0.95 \times S_D$. The distribution width of nearest-neighbor hopping coefficients and Hubbard U are shown in Figs. 14(b) and 14(c), respectively. In Fig. 14(d), we show the disorder dependence of the mean value of Hubbard U. It can be seen from the graph that $\langle u \rangle$ is not sensitive to the disorder strength.

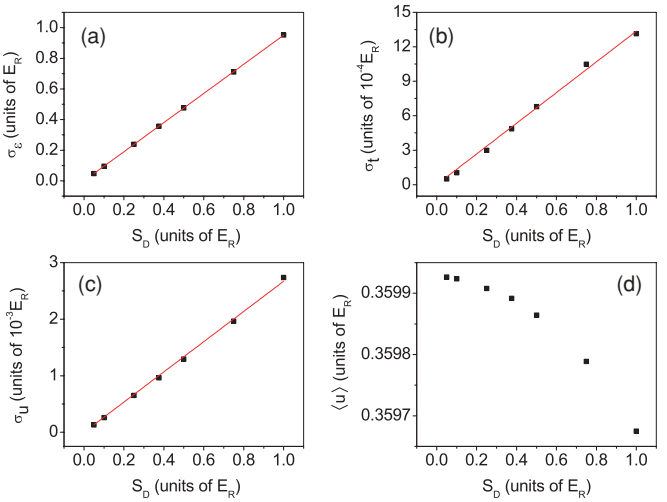

FIG. 14. (Color online) The width of the probability distribution for ϵ, t_{ij}, u_i, and $\langle u \rangle$ for $S_L = 14$.

V. CONCLUSION

In this article, we developed a method to construct low-energy basis states and applied the method to calculate the probability distributions of Hubbard model parameters in a disordered lattice created by an optical speckle field. The imaginary time projection method introduced in this article generates a type of Wannier-like localized basis that satisfies several conditions imposed by a reasonable coarse-grained, effective lattice Hamiltonian.

We compared the single-particle energy levels of the effective Hamiltonian with the exact Hamiltonian and found very good agreement, at least for weak disorder. Because we matched the single-particle density matrix in the continuum and lattice system, we expect that many-body properties will also be well reproduced. Detailed QMC calculations using the parametrized Hubbard model to compare with experimental measurements are in progress.

The method can be extended in several directions. When the disorder becomes strong enough, at some point, the assumption of one basis function per lattice site will be inadequate. For example, suppose that the potential in the region around one particular site gets sufficiently deep that its first excited state has a lower energy than the ground state energy of another site so that the bands overlap. Clearly the attractive site needs to be represented with two basis functions. Of course, if the atom-atom potential is repulsive, double occupation of the low-energy site will not be energetically favored. In this article, we have not explored the freedom of choosing the number of basis functions, their locations, and their detailed form.

A second extension of the method addresses strongly correlated many-body systems. In this article we calculated the Hubbard U using perturbation theory, for example, Eq. (28). However, this will be inadequate when the pair interaction distorts the single-particle orbitals. The formalism based on the thermal density matrix still applies, however, one has to work in the two-particle space, instead of in the single-particle space. This appears to be quite feasible and will be explored in a future publication, allowing one to calculate the Hubbard parameters even when perturbation theory is inaccurate.

ACKNOWLEDGMENTS

We thank R. M. Martin, B. L. DeMarco, F. Kruger, M. Pasienski, B. K. Clark, and Fei Lin for helpful discussions. This work has been supported with funds from the DARPA OLE Program.

[1] M. White, M. Pasienski, D. McKay, S. Q. Zhou, D. Ceperley, and B. DeMarco, Phys. Rev. Lett. **102**, 055301 (2009).
[2] O. F. Syljuåsen, Phys. Rev. E **67**, 046701 (2003).
[3] N. V. Prokof'ev, B. V. Svistunov, and I. S. Tupitsyn, JETP **87**, 310 (1998).
[4] G. H. Wannier, Phys. Rev. **52**, 191 (1937).
[5] M. R. Geller and W. Kohn, Phys. Rev. B **48**, 14085 (1993).
[6] N. Marzari and D. Vanderbilt, Phys. Rev. B **56**, 12847 (1997).
[7] I. Souza, N. Marzari, and D. Vanderbilt, Phys. Rev. B **65**, 035109 (2001).
[8] P. L. Silvestrelli, N. Marzari, D. Vanderbilt, and M. Parrinello, Solid State Commun. **107**, 7 (1998).
[9] P. H. Acioli and D. M. Ceperley, J. Chem. Phys. **100**, 8169 (1994).
[10] R. P. Feynman, *Statistical Mechanics* (Addison–Wesley, Reading, MA, 1998).
[11] P.-O. Löwdin, J. Chem. Phys. **18**, 365 (1950); P.-O. Löwdin, Adv. Quant. Chem. **5**, 185 (1970).
[12] H. F. Trotter, Proc. Am. Math. Soc. **10**, 545 (1959).
[13] J. G. Aiken, J. A. Erdos, and J. A. Goldstein, Int. J. Quant. Chem. **18**, 1101 (1980).
[14] U. Stephan and D. A. Drabold, Phys. Rev. B **57**, 6391 (1998).
[15] J. C. Slater, Phys. Rev. **87**, 807 (1952).
[16] J. W. Goodman, *Speckle Phenomena in Optics* (Roberts & Company Publishers, Greenwood Village, CO, 2006).